PAPER • **OPEN ACCESS**

X-ray mapping in a scanning transmission electron microscope of InGaAs quantum dots with embedded fractional monolayers of aluminium

To cite this article: T Walther *et al* 2020 *Semicond. Sci. Technol.* **35** 084001

OPEN ACCESS
IOP Publishing
Semiconductor Science and Technology
Semicond. Sci. Technol. **35** (2020) 084001 (10pp)
https://doi.org/10.1088/1361-6641/ab8c52

X-ray mapping in a scanning transmission electron microscope of InGaAs quantum dots with embedded fractional monolayers of aluminium

T Walther[1,5], J Nutter[2], J P Reithmaier[3] and E M Pavelescu[4,5]

[1] Kroto Centre for High Resolution Imaging and Analysis, Department of Electronic and Electrical Engineering, University of Sheffield, Mappin Building, Mappin Street, Sheffield S1 3JD, United Kingdom
[2] The Henry Royce Institute and Department of Materials Science and Engineering, University of Sheffield, Sir Robert Hadfield Building, Mappin Street, Sheffield S1 3JD, United Kingdom
[3] Technological Physics Department, Kassel University, Heinrich Plett Str. 40, 34132, Kassel, Germany
[4] National Institute for R&D in Microtechnologies, 126A Erou Iancu Nicolae, 077190 Voluntari, and Hyperion University, 169 Calea Calarasilor, Bucharest 030615, Romania

E-mail: t.walther@sheffield.ac.uk and emil.pavelescu@imt.ro

Received 23 January 2020, revised 8 April 2020
Accepted for publication 23 April 2020
Published 23 June 2020

Abstract

We investigate AlGaAs/GaAs superlattices as well as InGaAs/GaAs quantum wells and epitaxial quantum dots (QDs) where during the molecular beam epitaxy of InGaAs QDs the aluminium flux cell was opened briefly to incorporate fractional monolayers of Al into the InGaAs. We show that x-ray mapping with a large collection angle is capable of detecting 0.3–0.4 fractional Al monolayers with a resolution of just under 1 nm.

Keywords: scanning transmission electron microscopy, x-ray mapping, quantum wells, quantum dots, InGaAs

(Some figures may appear in colour only in the online journal)

1. Introduction

Energy-dispersive x-ray spectroscopy (EDXS) in a scanning transmission electron microscope (STEM) allows the direct chemical detection of all elements heavier than beryllium (or lithium, depending on detector entrance window type and spectrometer resolution) by local spectroscopy and compositional mapping at high spatial resolution. Many studies have been conducted over decades to improve quantification accuracy or spatial resolution.

Quantification in (S)TEM depends on the knowledge of the ionisation cross-sections of the chemical elements as a function of their atomic number (Z-effect) that was already modelled by Bethe in 1930 [1] and corrections for both absorption (A) of the x-rays in the specimen [2] and mutual fluorescence (F) between different x-ray lines [3]. This ZAF correction is still the basis of all commercial quantification procedures while new self-consistent iterative approaches such as the zeta-factor method [4] and thickness dependent k^* factors [5] have also recently been developed. Visibility of atomic lattice planes in x-ray maps has been reported after the incorporation of multiple x-ray detectors in transmission electron microscopes but only in rare cases of very thin non-periodic test structures [6–8] atomic resolution could really be verified. The corresponding maps were often too noisy for further quantification.

For semiconductor nanostructures embedded within or placed on top of thin foil specimens, additional geometrical corrections may be needed to evaluate line intensity ratios [9–13].

[5] Author to whom any correspondence should be addressed.

The University of Sheffield has recently acquired and installed a JEOL JEM-F200 cold field emission STEM with double windowless solid-state drift (SDD) detectors that yield x-ray collection angles of 1.0 and 0.7 srad (=1.7 srad in combination). This improves the statistics of x-ray mapping over the previous ultrathin-window Si:Li detectors with 0.12 srad (JEOL 2010 F at 197 kV) and 0.17 rad (JEOL Z3100 R005 at 300 kV) by an order of magnitude, enabling the detection and quantification of the atomic occupancy of semiconducting thin films consisting of single monolayers. Analysing the digital x-ray maps acquired with the JEOL Analysis Station software we highlight the improved performance for quantitative x-ray mapping and profiling but also problems related to spurious background signals and lack of valid *k*-factors.

2. Experimental

2.1. Epitaxial thin film growth

The motivation for this work is based on earlier results by other groups who showed that the optical emission of epitaxial InGaAs quantum dots (QDs) sandwiched between GaAs barriers can be tuned by replacing the GaAs below the QDs by either AlAs [14] or (InAlGa)As [15], or the GaAs cap on top by AlAs [16], or both lower and upper barriers by AlAs [17]. Here, we tried to incorporate ultra-thin AlAs layers *directly within* the InAs QDs.

The samples investigated in this work were grown on an n-type GaAs (001) substrate using a Varian Gen II solid-source molecular-beam epitaxy reactor. They resemble the central part of a laser structure and consist of an (Al)InGaAs-based active region surrounded by GaAs barriers, waveguide-like AlGaAs/GaAs superlattices and AlGaAs claddings. The growth temperature of the claddings and waveguide layers was 620 °C, while a lower temperature of 590 °C was used for the barriers. The active region was grown at 490 °C. Two samples were grown and labeled A527 and A558. The active region of sample A527 consists of InAlGaAs QDs deposited as seven individual repeats of alternating 0.124 nm $In_{0.14}Al_{0.28}Ga_{0.58}As$ followed by 0.112 nm InAs. The total nominal Al content deposited corresponded to 0.24 nm or 0.86 monolayer (ML) of the group III sub-lattice. The GaAs barriers were nominally 10 nm thick and growth interruptions of 90 s for change in growth temperature were introduced after the growth of the first 7 nm of the bottom barrier and the growth of first 3 nm of the top barrier. The waveguide-like superlattices consist of eight pairs of 2.4 nm GaAs followed by 2 nm $Al_{0.33}Ga_{0.67}As$, surrounding the barriers, and nine pairs of 1.7 nm GaAs and 2 nm $Al_{0.33}Ga_{0.67}As$. $Al_{0.33}Ga_{0.67}As$ cladding layers surround the superlattices. Another structure which leaves QDs uncovered on the free surface was repeated on top of the last AlGaAs cladding layer for giving access to the QDs morphology by AFM or SEM. The claddings, the superlattice waveguides and the barriers of sample A558 were similar in thickness, composition and growth temperature to those of the A527 sample, except for the active region. This consisted of a 7 nm $In_{0.25}Ga_{0.75}As$ quantum well deposited after the growth of the first 10 nm GaAs barrier, followed by a 2 nm GaAs spacer layer on top of which $In_{0.6}Ga_{0.4}As$ QDs with insertion of a very thin Al layer were deposited before the top 10 nm barrier was eventually grown. The QDs were grown by depositing nine individual layers of equal thickness (0.2 nm) of material, as thus: first we deposited two layers consisting of 0.1 nm $In_{0.2}Ga_{0.8}As$ and 0.1 nm of InAs each, then one repeat of 0.12 nm $In_{0.34}Al_{0.66}As$ and 0.08 nm InAs, then another six repeats similar to the first two. As in the case of A527, the last 3 nm of the bottom GaAs barrier, the quantum well (QW), the GaAs spacer, the QDs and the first 3 nm of the top GaAs barrier were all grown at the same temperature of 490 °C. An overview of both structures is presented in table 1.

Table 1. Schematic of both samples. QD = quantum dot, QW = quantum well.

sample		A527	both	A558
thick-ness [nm]	material			
1.65	InGaAs + Al	QD		QD
2	GaAs	—		spacer
7	InGaAs	—		QW
10	GaAs		barrier	
2.4/2.0	GaAs/AlGaAs		superlattice 8x	
1.7/2.0	GaAs/AlGaAs		superlattice 9x	
20	AlGaAs		cladding	
1.7/2.0	GaAs/AlGaAs		superlattice 9x	
2.4/2.0	GaAs/AlGaAs		superlattice 8x	
10	GaAs		barrier	
1.65	InGaAs + Al	QD		QD
2	GaAs	—		spacer
7	InGaAs	—		QW
10	GaAs		barrier	
2.4/2.0	GaAs/AlGaAs		superlattice 8x	
1.7/2.0	GaAs/AlGaAs		superlattice 9x	
20	AlGaAs		cladding	
150	GaAs		buffer	
	GaAs		substrate	

2.2. Specimen preparation for electron microscopy

Electron transparent thin foils were prepared by glueing together wafer pieces using two-component epoxy glue, cutting with a diamond impregnated wire saw along <110> directions, grinding by SiC abrasive and polishing with 3 μm and finally 1 μm diamond paste. The cross-sections were then argon ion milled in either a Technoorg Linda IV3 under liquid nitrogen cooling or a Gatan PIPS ion mill, at angles of $\sim$5° and energies of initially 4 keV until perforation, then 2 keV and finally 0.5 keV.

2.3. STEM characterization

The scanning transmission electron microscopy (STEM) imaging was performed in two instruments: a JEOL 2010 F (Schottky field emitter, 197 kV, 10 mrad semi-angle of beam convergence, 0.3 nm probe, $\sim$20 pA current at nominal spot size M, 55–170 mrad collection angle in high-angle annular

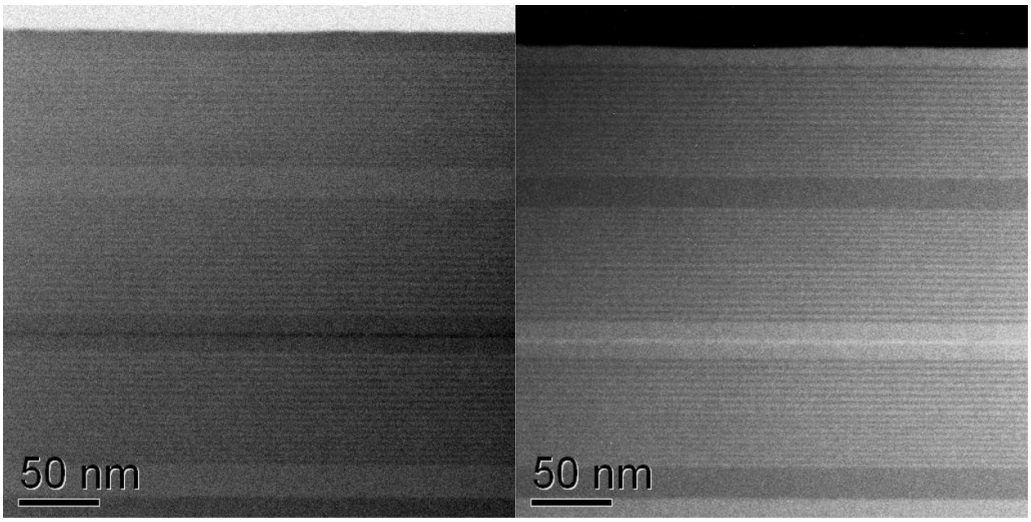

Figure 1. Bright field (BF, left) and annular dark field (ADF, right) images of sample A527. Overview of the layer stack at 200 kX. Visible are the outermost 19 nm AlGaAs cladding layers (dark in ADF), several 32 nm and 34 nm thick 8 × AlGaAs/GaAs superlattices and two 8 nm and 10 nm GaAs barriers that sandwich a ∼3 nm thin central InGaAs layer (bright in ADF).

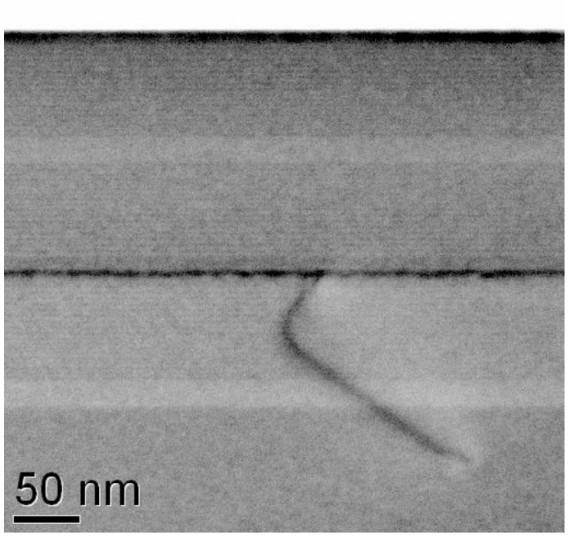

Figure 2. BF image of sample A527 at 150 kX. The sample is thinner here and clearly shows strain modulations characteristic of strained quantum dots, as well as a dislocation line emanating from the strained InGaAs quantum dot layer.

dark field (HAADF) mode, Si:Li PentaFET x-ray detector with 0.12 srad collection angle and ultrathin window) and a JEOL F200 (cold field emitter, 200 kV, 20 mrad semi-angle of convergence, 0.16 nm probe, ∼100 pA current at nominal spot size 6, 45–165 mrad HAADF collection angle, 1.7 srad windowless double silicon drift detectors for x-rays). All images and maps were acquired with the layers oriented vertical to minimize both scan and drift artifacts and are displayed in the following rotated by 90° so that the growth direction points upwards.

The images in figure 1 of sample A527 show layers as described in the nominal stack design, with apparently perfect GaAs/AlGaAs superlattices but two deviations from the nominal design: the AlGaAs cladding layers are only 19 nm wide, and the (In,Al,Ga)As has formed a continuous ∼3 nm thin slightly corrugated quantum well with slight lateral variations, however, as the specimen foil thickness is relatively large, it is not possible to reliably distinguish a continuous quantum well from a series of dots in projection. In some cases dislocations emanating from the InAlGaAs layer have been found (cf figure 2). The surface of the wafer could not be analysed in detail here and no clear evidence of any quantum dots there was found. In ADF mode the intensity depends almost linearly on the specimen thickness and approximately quadratically on the average atomic number (Z) of the material, and this is often referred to as Z-contrast [18]. Hence, indium rich layers in (Al,Ga,In)As appear bright in ADF, and the square root of their ADF intensity is a signal approximately proportional to the local chemical composition and to the sample thickness [19] if the inner collection angle is sufficiently large [20].

The dislocation shown in figure 2 runs through the superlattices and cladding layer into the buffer region where it terminates on the specimen surface. As buffer, cladding layer and superlattices are all made of AlGaAs lattice matched to GaAs, while the InGaAs that has a larger lattice constant is compressively strained, we can conclude that if the dislocation relaxes strain it is likely to have generated at a quantum dot.

The x-ray maps in figures 3(b)–(f) depict the spatial distribution of elements in a specimen estimated from tilting experiments to be ∼30 nm thin (for details see section 3). The indium rich QW/QD layer in the centre, surrounded by first GaAs barriers and then the AlGaAs/GaAs superlattices, is visible, as well as, very faintly in figure 3(e), an enrichment of Al approximately at the same height where a dark band can be seen running through the InGaAs layer in figure 3(a). The nearly featureless maps of As in figure 3(d) and of Al + Ga + In in figure 3(g) are very similar and indicate that the effect of different relative fluorescence yields of the various x-ray lines (often referred to as k-factors [21]) deviate from unity by only a few % relative and so are negligible here. Table 2 shows

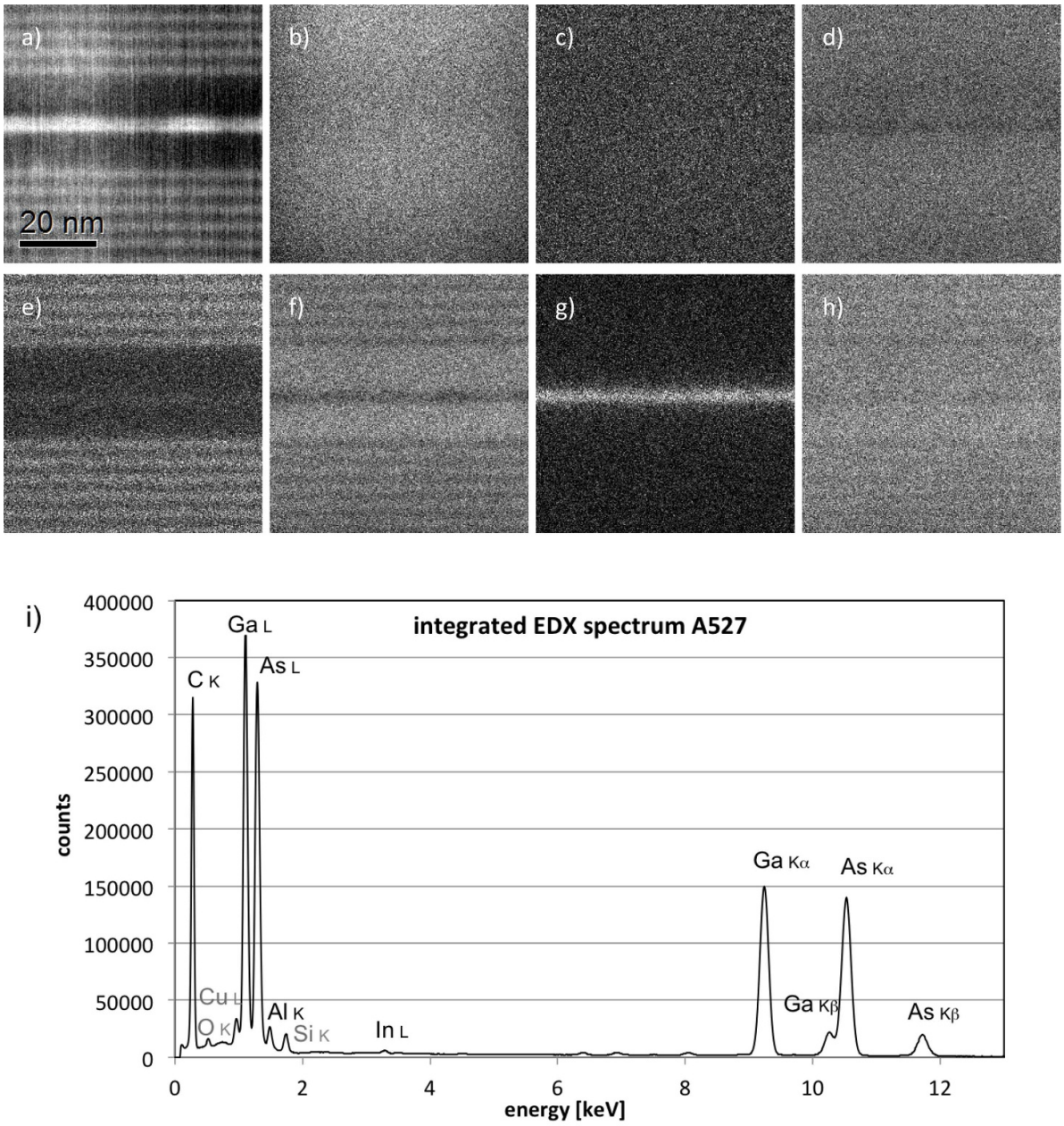

Figure 3. ADF image (a) and x-ray maps recorded of sample A527 at 3MX, 67 nm field of view, 0.26 nm pixel^{-1} sampling. 256^2 pixels, 0.16 nm probe, 0.1 nA, 0.2 ms dwell time, 52 sweeps with drift correction for 12 min, 13 kcps from detector #1 and 15 kcps from detector #2. The maps show the net signals of C_K (b), O_K (c), As_K (d), Al_K (e), Ga_K (f), In_L (g) and the sum of all group III elements (h = e + f + g). (i) Integrated x-ray spectrum from figure (a) on linear scale.

that maps of elements not in the specimen of sample A527 but present in the specimen support (Cu), or specimen holder and objective lens (Fe, Co) yield featureless maps of 1.3–1.6 counts per pixel on average. O from surface contamination (2.7 ± 1.6 counts) and Si from the detector material itself (3.5 ± 1.8 counts) are slightly higher but also close to the overall detection limit and reveal no structure. Whether the pervasive background signal of ∼1.3 counts in all maps is due to real bremsstrahlung reaching the x-ray detectors or a detector artifact, is still under investigation, however, it has been shown previously that for accurate quantification it is important to subtract off even such low background signals using fractional counts [22]. Figure 4 compares profiles of Al and In (divided by the sum of Al + Ga + In to normalize with respect to occupancy of the group III sub-lattice) without and with an average of 1.3 counts subtracted from each map.

The Al content of the 4.5 nm period superlattice varies by only about $\Delta y_{Al} = 0.08$ (between $Al_{0.07}Ga_{0.93}As$ and $Al_{0.15}Ga_{0.85}As$, depending on background removal) and is thus much lower than the nominal Al content of the barrier layers. Also, the ∼10 and ∼12 nm wide layers around the quantum dots layer appear to be not pure GaAs but AlGaAs with a low Al content of 0.04 ± 0.01, with a slight local increase by 0.02–0.03 near the lower side of the InGaAs. This bump

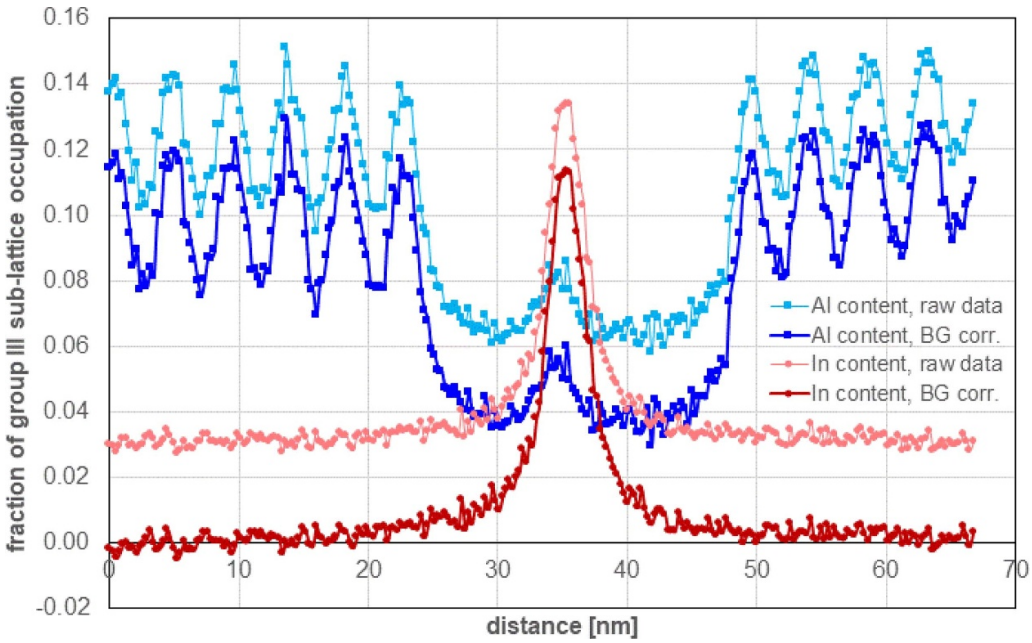

Figure 4. Line profiles of the ratios of the x-ray maps of Al/(Al + Ga + In) and In/(Al + Ga + In) for sample A527 without any background correction (raw data) and after 1.3 counts subtracted from each map prior to ratio calculation (BG corrected). Neglecting *k*-factors for x-ray fluorescence and absorption, these yield only approximate values of the corresponding fractional occupancies of the group III sub-lattice at ∼1 nm resolution. Note the InGaAs QD layer and the local Al increase by ∼0.02 in the centre are displaced laterally by two data points, i.e. 0.5 nm (approximately a unit cell).

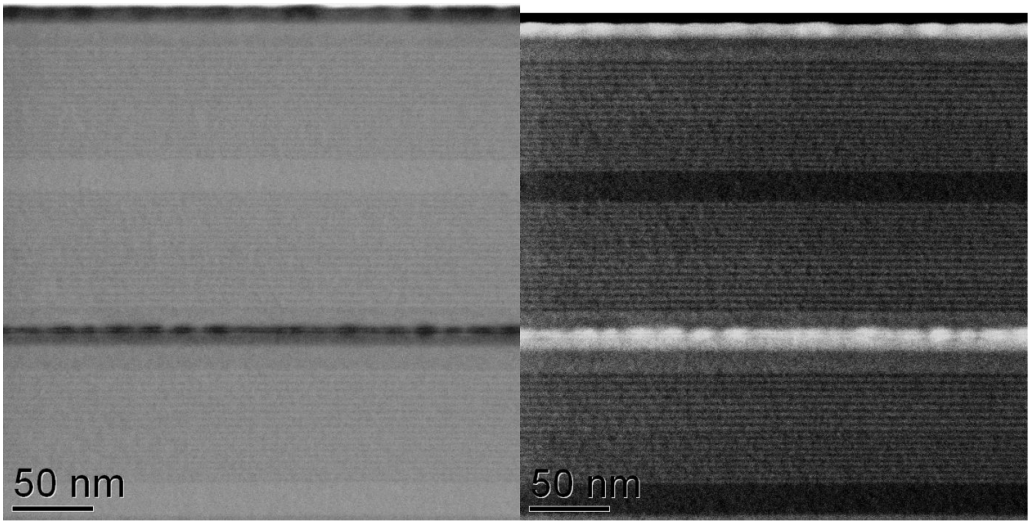

Figure 5. BF (left) and ADF (right) images of sample A558. Overview of the layer stack at 200 kX. The 19 nm AlGaAs cladding layers (dark in ADF) and 32 nm and 34 nm AlGaAs/GaAs superlattices are as in the other sample. The two GaAs barriers are 14 nm and 9 nm thin; the central InGaAs (bright in ADF) now consists of clearly two layers, a flat InGaAs QW and a QD layer atop.

amounts to an additional Al coverage of 0.3 equivalent monolayers when integrated above the background level of 0.035. The quantum dot layer itself has a maximum indium content of $x_{\mathrm{In}} = 0.12 \pm 0.02$, again lower than nominal.

The images in figure 5 are from sample A558 and again show that the AlGaAs cladding layers are ∼19 nm thick, the lower GaAs layer is 15 nm, the middle GaAs 1 nm and the top 12 nm thick. The lower $In_xGa_{1-x}As$ quantum well (nominal $x_{\mathrm{In}} = 0.25$) in the central stack is ∼7 nm thick as specified but shows a significant In segregation towards its top, yielding an indium concentration close to that of the upper In(Al)GaAs layer (nominal $x_{\mathrm{In}} = 0.60$). Both In(Al)GaAs layers exhibit strong lateral contrast modulations which are correlated between the lower InGaAs and the upper In(Al)GaAs layers, indicating a degree of strain coupling. In the top In(Al)GaAs layer of the central stack quantum dots are now clearly visible, in line with what is expected from Stranski-Krastanow growth of InGaAs [23]. Near the free surface, a rather diffuse and slightly corrugated In(Al)GaAs layer has been formed where the intended quantum dots are clearly less well developed. Figure 6 is a close-up ADF image at higher magnification of the QD structure of A558. The sample has

Table 2. Statistics of counts of x-ray maps. rms = root mean square (standard deviation). Type: n = noise, s = true signal,? = possible signal due to surface contamination (C), oxidation (O) or argon incorporation due to ion milling (Ar).

sample		A527	- >			A558	- >			
element	x-ray line	min	max	mean	rms	min	max	mean	rms	type
C	K	7	53	26.6	±5.7	96	320	198.4	±28.3	?
O	K	0	13	2.7	±1.6	0	10	1.8	±1.4	?
Ne	K	0	14	3.5	±1.9	0	9	1.5	±1.2	n
Al	K	0	20	4.7	±2.5	0	32	9.5	±4.6	s
Si	K	0	15	3.5	±1.9	0	16	5.5	±2.8	n
Ar	K	0	9	1.5	±1.2	0	7	0.7	±0.8	?
Ti	K	0	9	1.3	±1.2	0	7	0.7	±0.8	n
Fe	K	0	9	1.5	±1.2	0	8	0.9	±0.9	n
Co	K	0	9	1.6	±1.3	0	8	0.8	±0.9	n
Cu	K	0	9	1.6	±1.3	0	8	0.8	±0.9	n
Ga	K	14	70	38.7	±6.6	24	112	61.8	±13.4	s
As	K	17	76	39.6	±6.4	20	112	60.5	±12.7	s
In	L	0	15	1.8	±1.6	0	32	3.8	±4.3	s

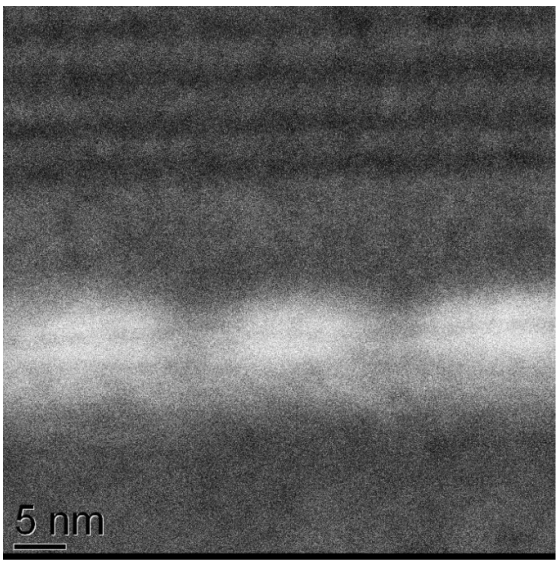

Figure 6. ADF image of sample A558 at 1 MX. The InGaAs layer is clearly structured, with a 5–8 nm quantum well at the bottom, followed by ∼5 nm high quantum dots that have a dark line running approximately through their centres (which figure 7 confirms is due to Al incorporation).

also been studied by x-ray mapping as the one before, and results are shown in figures 7 and 8. Again, an increase of the Al signal under the InGaAs is found; its integral above the background level of ∼0.06 amounts to 0.4 ml half of which is located directly under the InGaAs QD while the other half appears to be more spread out.

3. Result and discussion

A central problem of quantifying x-ray maps is low count rates due to short dwell times at individual pixels, even with larger and multiple x-ray detectors. Table 2 lists the statistics of the x-ray maps shown in figures 3 (sample A527) and 7 (sample A558).

Table 3. *K*-factors of x-rays of group III elements (index j) relative to As K line, multiplied by A_{As}/A_j.

			CASINO	JEOL
model				
element	x-ray line	A_j	$k_{j,AsK} \cdot 74.92/A_j$	
Al	K	26.98	0.883 ± 0.106	0.996
Ga	K	69.72	1.051 ± 0.011	0.916
In	L	114.8	0.961 ± 0.018	0.838

In order to estimate the spatial resolution we have tried to determine the thickness more accurately combining two different approaches, one based on geometry and one based on analyzing spectral count rates, as follows: the areas investigated were about 160 nm (A527) and 100 nm (A558) away from the specimen edge. For a perfect 10° wedge geometry (as the ion beam impinged under 5° on both surfaces) this would give thickness estimates of 28.0 nm and 17.5 nm, respectively, but such perfect wedges can rarely be achieved. Often, samples are more rounded at the edges. The thickness *difference* between the two areas should however remain to be 10.5 nm, even with rounded edges. From the spectra taken in succession without changing the electron beam current we can work out the x-ray count rates as 14 114 s^{-1} (A527) and 8385 s^{-1} (A558) and can thus conclude that the thickness *ratio* should be 1.683:1, i.e. the second area has only 59.4% the thickness of the first. Combining this with the above information gives absolute thickness values of 25.9 nm for A527 and 15.4 nm for A558. Using the standard formulas for electron beam broadening [24, 25] then suggests beam broadening of 1.2 nm for the 26 nm thick area of sample A527 and 0.5–0.6 nm for the 15.4 nm thin area of A558. We have cross-checked this with previous Monte Carlo calculations of the Ga K/L line ratio for InGaAs samples using an ideal Si:Li detector with ultrathin polymer window as was appropriate for our JEOL 2010 F [26]. For the windowless SDD detectors used here, the Ge L count rate will go up as a ∼300 nm thick carbon layer would no longer absorb ∼18% of this x-ray line. At the same time the Ge K count rate will go

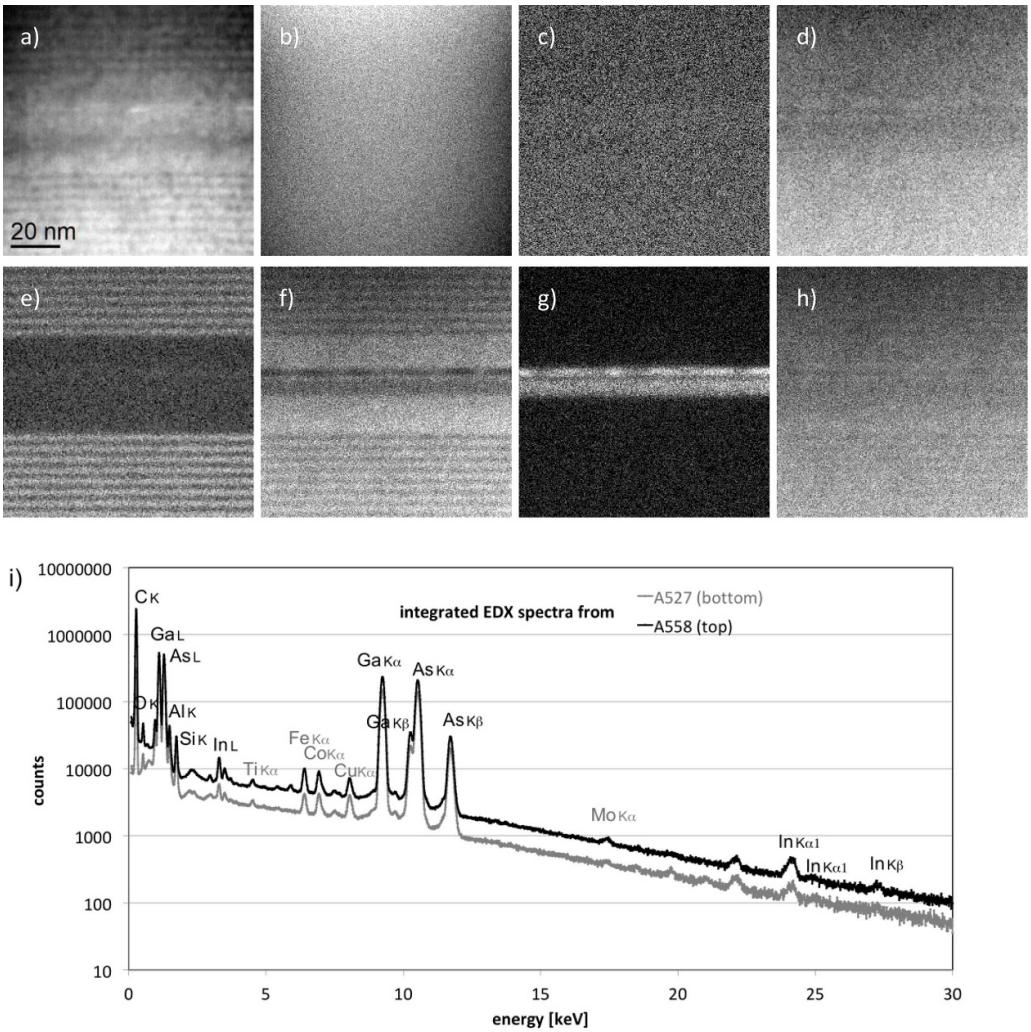

Figure 7. ADF image (a) and x-ray maps of A558 recorded at 2 MX, 100 nm field of view, 0.195 nm pixel^{-1}. 512^2 pixels (2x binned to 256^2 pixels at 0.39 nm pixel^{-1}), 0.16 nm probe (spot size 6), 0.1 nA, 0.2 ms dwell time, 61 sweeps with drift correction in 53 min, 4 kcps from detector #1 and 6 kcps from detector #2. The maps show the net signals of C_K (b), O_K (c), As_K (d), Al_K (e), Ga_K (f), In_L (g) and the sum of all group III elements (h = e + f + g). The quantum dots are better visible in (g) than in (a) because this sample is very thin. (i) Integrated x-ray spectra from areas shown in figures 7(a) and 3(a) on logarithmic scale.

down by ∼2% because the silicon in SDD detectors has only the typical wafer thickness of 0.5 mm so some hard x-rays can penetrate it. We can hence use previous plots of Ga K/L ratio vs thickness if we re-calibrate the value for zero thickness to be 0.81 times the value of 1.20 for Si:Li, i.e. 0.97. The Ga K/L ratios we actually measured in our spectra of 0.973 and 1.027 would then suggest thicknesses of around 4 nm and 28 nm, respectively, which are in reasonable agreement with the above estimates, given the relative large errors of this approach.

We have then used Monte Carlo simulations [27] for 200 keV electrons to further investigate x-ray generation, absorption, fluorescence and detection at a take-off angle of 25°.

Simulations of x-ray absorption for AlInGaAs samples at thicknesses of 16–28 nm show that no absorption correction needs to be included for Ga K and In L lines relative to As K, the only slightly affected x-ray being the softer Al K line whose intensity is expected to decrease by 7%–8% and so would need an absorption correction factor of 1.07 ± 0.02.

Mutual fluorescence that could increase the Al K line intensity has ben studied by a series of simulations of x-ray generation on InGaAs samples of varying thickness with a thin AlAs layer in the centre sandwiched between GaAs at the bottom and either InAs or GaAs in the top half. We considered thicknesses from 10 to 600 nm. We evaluated the fluorescence from the In L onto the Al K line by comparing the apparent increase in Al x-ray intensity when the GaAs overlayer was replaced by InAs and found that in the thickness range of 10–40 nm relevant for our experiments the effect was hardly detectable (maximal 1.8% relative increase at 40 nm for 16 nm pure InAs on top) and so we conclude that mutual fluorescence is negligible in our samples that are very thin and wherein both the overall In and Al content are much lower.

This means that quantification can be performed using the standard thin-film approximation first used by Cliff and

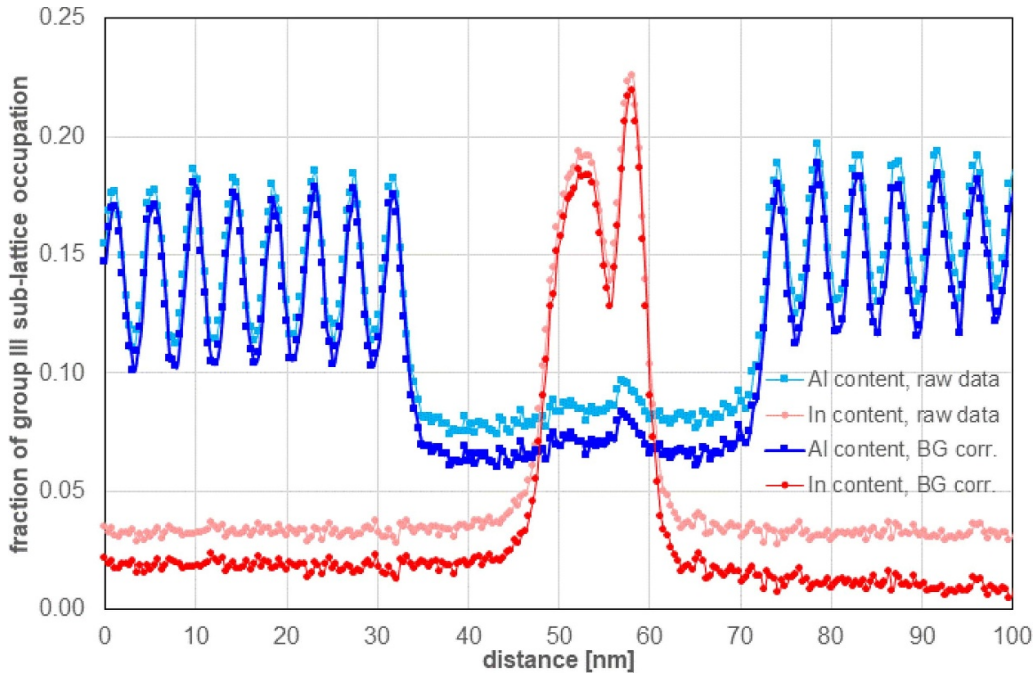

Figure 8. Line profiles of the ratios of the raw x-ray maps of Al/(Al + Ga + In) and In/(Al + Ga + In) for sample A558. Again, a strong Al increase coincides with the start of the QD layer growth while perhaps a fainter signal is visible near the start of the QW layer underneath.

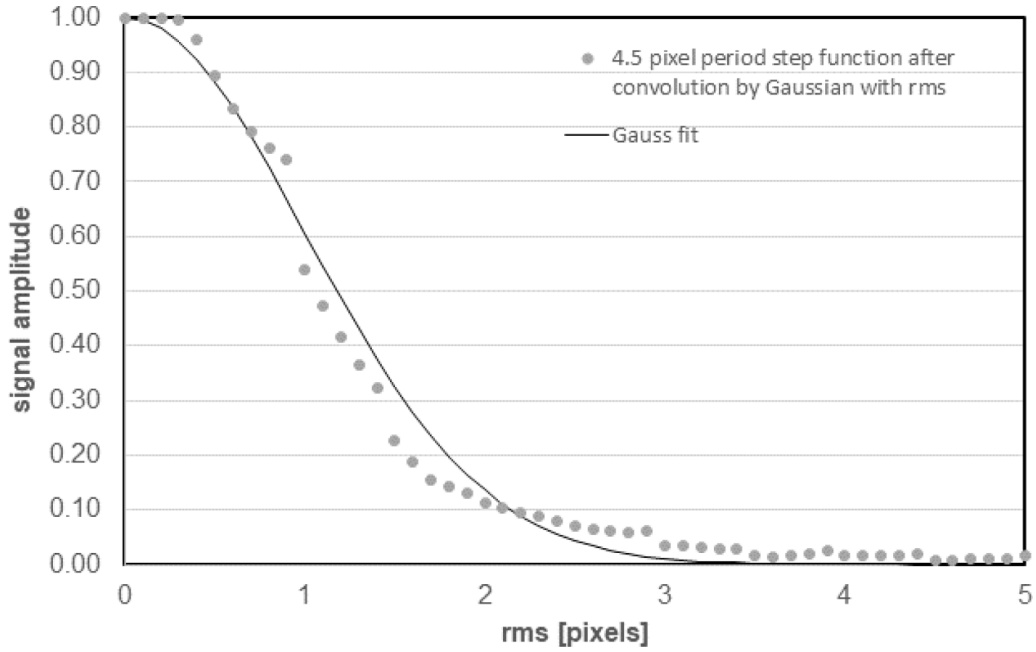

Figure 9. Numerical simulation of the effect of resolution upon signal amplitude of a 4.5 pixel ideal 1D step function when convoluted with a 2D Gaussian of given root-mean-square (rms) value. For the AlGaAs/GaAs superlattice, set 1 nm = 1 pixel to evaluate.

Lorimer [21]. For quantifying x-ray spectra from thin samples the intensities, I, of an individual line chosen for each element (index j) should be multiplied by their k-factors and, if these are calibrated for weight fractions, divided by the corresponding atomic weights A so that

$$x_j = \frac{I_j k_j / A_j}{\sum_n I_n k_n / A_n} \qquad (1)$$

gives the concentration of element j in thin film approximation where the sum extends over all n elements. We have in the plots of figures 4 and 8 completely neglected k-factors because the scale factors k_j/A_j are all close to unity for the (Al,Ga,In)As system if the common As K–line (As_K) is used for reference: from extrapolating Monte Carlo simulations for AlGaAs and InGaAs back to zero thickness, and taking into account the same modifications as before to replace a thick Si:Li with

ultrathin polymer window by a windowless SDD detector, we get $k_{\mathrm{AlK,AsK}} = 0.32 \pm 0.04$, $k_{\mathrm{GaK,AsK}} = 0.98 \pm 0.01$ [26] and $k_{\mathrm{InL,AsK}} = 1.47 \pm 0.03$ [28]. Using the nominal k-factors of the JEOL supplied software instead would give $k_{\mathrm{AlK,AsK}} = 0.359$, $k_{\mathrm{GaK,AsK}} = 0.853$, $k_{\mathrm{InL,AsK}} = 1.284$. The k-factors in equation (1) need to be divided by the atomic weights and then divided by $k_{\mathrm{AsK}}/A_{\mathrm{A,}}$ i.e. the above values for $k_{\mathrm{j,AsK}}$ need to be multiplied by the relative atomic weights $A_{\mathrm{As}}/A_{\mathrm{j}}$. The results are tabulated in table 3.

This means the real Al and In content could have been a little lower than shown in the plots, but given the poor statistics and that the use of the above correction factors would only marginally improve the ratio of all group III elements to arsenic (which should yield unity but is always above that value), we decided to neglect this correction.

All linescans clearly reveal the shorter AlGaAs/GaAs superlattice (of period 4.5 nm) and the measured full widths at half maximum (FWHM) values of the narrowest individual layers prove that the resolution must be 2 nm or better in both cases. Concerning the influence of resolution on the contrast of maps and linescans three effects should be considered:

(i) the sampling increment given by the effective pixel width, here 0.26 nm in the first and 0.39 nm (after binning) in the second case;
(ii) the impinging focused electron probe profile (here: 0.16 nm FWHM, giving an rms width of approximately $\sigma_{\mathrm{p}} = 0.07$ nm in Gaussian approximation);
(iii) the broadening of the electron in the sample due to multiple elastic scattering, as evaluated before.

While effect (ii) will be negligible in our case (the above rms width corresponding to only 0.18–0.26 pixels would dampen the signal from the superlattice by 6% at the most, according to the plot in figure 9), electron beam scattering in (iii) will dominate the effective resolution. This can be shown by again evaluating models for electron probe spreading, which for 15–26 nm thin GaAs ($<Z \geqslant 32$, $\sigma = 5.32$ g cm^{-3}, $U = 200$ kV) suggest $b = 1.4$ nm for the 1.9σ beam diameter that contains 90% of intensity [29] (i.e. $\sigma_{\mathrm{b}} = 0.74$ nm) or $b = 0.5$–1.2 nm for the full beam diameter at the exit surface [25] (hence, $\sigma_{\mathrm{b}} = 0.2$–$0.5$ nm for an equivalent Gauss function). These values are larger than the nominal probe σ_{p} and would dampen the apparent superlattice modulation of the Al content by 10%–20% of the nominal value of $\Delta y_{\mathrm{Al}}{}^{\mathrm{nom}} = 0.33$, i.e. bring it down to 0.26. We measure, however, only an amplitude of $\Delta y_{\mathrm{Al}}{}^{\mathrm{exp}} = 0.08$, which indicates that there must be real interdiffusion of Al within the superlattices, corresponding to an rms diffusion length for Al atoms of $\sim$1.5 nm.

The peak indium concentrations x_{In} measured are also somewhat lower than the nominal values (0.19 instead of 0.25 for the lower QW of sample A558, 0.12 [0.22] for the QDs instead of 0.55 [0.60] for sample A527 [558]), which again indicates some indium interdiffusion, but only over $\sim$0.5 nm in length, in line with our resolution estimate.

The concentration profiles from the group-III elements Al and In in figure 8 show essentially the same features as before for the other specimen, but this time with significantly higher In concentration (albeit still below the nominal values). The bump in the Al profile correlates with the InGaAs QD layer, with their respective peaks shifted by three pixels, or 1 nm. The relative displacement of the In signal compared to the Al signal by 0.5–1 nm towards the top of the wafer structure indicates stronger surface segregation of In compared to Al atoms. This finding for MBE growth of (Al,In)GaAs differs from our previous findings for chemical vapour epitaxy of (Al,In)GaN [30].

A key problem has been that the maps never gave zero base line values for elements not in the sample. We therefore used the minimum experimental background found for any element not in the sample (Ti K) to subtract 1.3 and 0.7 counts for the two different samples. This worked well for the In L line but less so for the Al K line, and we need to investigate further whether this problem is due to insufficient shielding to stray x-rays (a possible collimator problem), the line fitting routine used (a software problem) or simply due to the fact that all signals recorded are positive definite (i.e. non-negative) maps that cut off small negative while retaining small positive values, thereby skewing and offsetting the background by some artificial small amount.

4. Conclusion

X-ray maps have been quantitatively evaluated for all elements of the group-III sub-lattice and direct evidence for 0.3–0.4 equivalent monolayers of Al deposited close to the middle of the InGaAs quantum dots has been found.

Acknowledgments

We wish to acknowledge the Henry Royce Institute for Advanced Materials, funded through EPSRC Grant Nos. EP/R00661X/1, EP/S019367/1, EP/P02470X/1 and EP/P025285/1, for the financial support for JN and for access to the JEOL JEM-F200. E M Pavelescu acknowledges the PCCDI 75/2018 VARDIMTECH (PN-III-P1-1.2-PCCDI −2017-0152) Project.

ORCID iD

T Walther https://orcid.org/0000-0003-3571-6263

References

[1] Bethe H 1930 Zur theorie des durchgangs schneller korpuskularstrahlen durch materie *Ann. Phys.* **397** 325–400
[2] Philibert J 1963 A method for calculating the absorption correction in electron-probe microanalysis *Proc. Int. Symp. X-ray Optics and X-ray Microanalysis*, ed H H Pattee, V E Cosslett and E Engström (New York: Academic) p 379
[3] Reed S J B 1965 Characteristic fluorescence corrections in electron-probe microanalysis *Brit. J. Appl. Phys.* **16** 913–26

[4] Watanabe M, Horita Z and Nemoto M 1996 Absorption correction and thickness determination using the zeta factor in quantitative x-ray microanalysis *Ultramicroscopy* **65** 3–4, 187–98
[5] Walther T 2010 An improved approach to quantitative x-ray microanalysis in (S)TEM: thickness dependent *k*-factors *J. Phys. Conf. Ser.* **241** 012016
[6] von Harrach H S, Dona P, Freitag B, Soltau H, Niculae A and Rohde M 2010 An integrated multiple silicon drift detector system for transmission electron microscopes *J. Phys. Conf. Ser.* **241** 012015
[7] Allen L J, D'Alfonso A J, Freitag B and Klenov D O 2012 Chemical mapping at atomic resolution using energy-dispersive x-ray spectroscopy *MRS Bull.* **37** 47–52
[8] Ohnishi I, Suzuki T, Miyatake K, Jimbo Y, Iwasawa Y, Morita M, Sasaki T, Sawada H and Okunishi E 2018 Analytical and in situ applications using aberration corrected scanning transmission electron microscope *e-J. Surf. Sci. Nanotechnol.* **16** 286–8
[9] Bangert U, Harvey A J, Dieker C, Hartmann A and Keyse R 1996 Highly spatially resolved X-ray analysis of semiconductor alloys and nanostructures in a scanning transmission electron microscope *Philos. Mag.* A **74** 1421–37
[10] Zhi D, Davock H, Murray R, Roberts C, Jones T S, Pashely D W, Goodhew P J and Joyce B A 2001 Quantitative compositional analysis of InAs/GaAs quantum dots by scanning transmission electron microscopy *J. Appl. Phys.* **89** 2079–83
[11] Walther T 2010 Comparison of experimental and theoretical x-ray intensities from (In)GaAs specimens investigated by energy-dispersive x-ray spectroscopy in a transmission electron microscope *J. Phys. Conf. Ser.* **209** 012029
[12] Amari H, Lari L, Zhang H Y, Geelhaar L, Cheze C, Kappers M J, McAleese C, Humphreys C J and Walther T 2011 Accurate calibration for the quantification of the Al content in AlGaN epitaxial layers by energy-dispersive x-ray spectroscopy in a transmission electron microscope *J. Phys. Conf. Ser.* **326** 012018
[13] Bender H, Seidel F, Favia P, Richard O and Vandervorst W 2017 X-ray absorption in pillar-shaped transmission electron microscopy specimens *Ultramicroscopy* **177** 58–68
[14] Kim J S *et al* 2001 Energy level control of self-assembled InAs quantum dots utilizing an thin AlAs layer *Appl. Phys. Lett.* **78** 3247–9
[15] Wei Y Q, Wang S M, Ferdos F, Vukusic J, Zhao Q X, Sadeghi M and Larsson A 2003 Aluminium incorporation for growth optimization of 1.3μm emission InAs/GaAs quantum dots by molecular beam epitaxy *J. Cryst. Growth* **215** 172–6
[16] Ferdos F, Wang S, Wei Y, Sadeghi M, Zhao Q and Larsson A 2003 Influence of initial GaAs and AlAs cap layers on InAs quantum dots grown by molecular beam epitaxy *J. Cryst. Growth* **251** 145–9
[17] Jung S I *et al* 2005 Bandgap engineering of self-assembled InAs quantum dots with a thin AlAs barrier *Physica* E **26** 100–4
[18] Pennycook S J and Jesson D E 1991 High-resolution *Z*-contrast imaging of crystals *Ultramicroscopy* **37** 14–38
[19] Qiu Y, Lari L, Ross I M and Walther T 2011 Comparison of the contrast in conventional and lattice resolved ADF STEM images of InGaAs/GaAs structures using different camera lengths *J. Phys. Conf. Ser.* **326** 012041
[20] Walther T 2006 A new experimental procedure to quantify annular dark field images in scanning transmission electron microscopy *J. Microsc.* **221** 137–44
[21] Cliff G and Lorimer G W 1975 Quantitative analysis of thin specimens *J. Microsc.* **103** 203–7
[22] Wang X, Bai J and Walther T 2018 Self-consistent absorption correction for quantification of the indium and aluminium content from noisy x-ray maps of group III nitride nanowires *J. Microsc.* **272** 111–22
[23] Walther T, Cullis A G, Norris D J and Hopkinson M 2001 Nature of the Stranski-Krastanow transition during epitaxy of InGaAs on GaAs *Phys. Rev. Lett.* **86** 2381–4
[24] Williams D B and Carter C B 1996 *Transmission Electron Microscopy: IV Spectrometry* (Berlin: Springer)
[25] Walther T 2004 Development of a new analytical electron microscopy technique to quantify the chemistry of planar defects and to measure accurately solute segregation to grain boundaries *J. Microsc.* **215** 191–202
[26] Walther T and Wang X 2016 Self-consistent method for quantifying indium content from x-ray spectra of thick compound semiconductor specimens in a transmission electron microscope *J. Microsc.* **262** 151–6
[27] Drouin D, Couture A R, Joly D, Tastet X, Aimez Y and Gauvin R 2007 CASINO v2.42.—a fast and easy-to-use modeling tool for scanning electron microscopy and microanalysis users *Scanning* **29** 92–101
[28] Parri M C, Qiu Y and Walther T 2015 New pathways for improved quantification of energy-dispersive x-ray spectra of semiconductors with multiple x-ray lines from thin foils investigated in transmission electron microscopy *J. Microsc.* **260** 427–41
[29] Goldstein J I, Costley J L, Lorimer G W and Reed S J B 1977 Quantitative x-ray analysis in the electron microscope *Scanning Electr. Microsc.: Proc. Workshop Anal. Electron Microsc. (Chicago)* **1** 315–24
[30] Walther T, Amari H, Ross I M, Wang T and Culli A G 2013 Lattice resolved annular dark-field scanning transmission electron microscopy of (Al,In)GaN/GaN layers for measuring segregation with sub-monolayer precision *J. Mater. Sci.* **48** 2883–92